

Received July 4, 2019, accepted July 27, 2019, date of publication August 1, 2019, date of current version August 19, 2019.

Digital Object Identifier 10.1109/ACCESS.2019.2932427

An ICI Suppression Analysis Testbed for Harbor Unmanned Ground Vehicle Deployment

TIEN HOA NGUYEN¹, THANH HIEU NGUYEN², TAEHYUN YOON³,
WOO-SUNG JUNG³, DAESEUNG YOO³, AND SOONGHWAN RO⁴

¹School of Electronics and Telecommunications, Hanoi University of Science and Technology (HUST), Hanoi 100000, Vietnam

²Nanyang Technological University, Singapore 639798

³Electronics and Telecommunications Research Institute (ETRI), Daejeon 34129, South Korea

⁴Kongju National University, Cheonan 31080, South Korea

Corresponding author: Taehyun Yoon (thyoon0820@etri.re.kr)

This work was supported by the Electronics and Telecommunications Research Institute (ETRI) through the Korean Government — the development of smart context-awareness foundation technique for major industry acceleration under Grant 19ZS1300 and the development of smart HSE and digital cockpit systems based on ICT convergence for enhanced major industry under Grant 19AS1100.

ABSTRACT In recent years, intelligent transport system (ITS) applications with unmanned ground vehicles (UGV) have increased dramatically to improve the safety, efficiency, and unique services in low-to medium-range communication deployment. Orthogonal frequency division multiplexing (OFDM) is adopted as a modulation scheme for this communication system to combat fading. Unfortunately, because of possible high UGV speed, the orthogonality between subcarriers in OFDM signals is prone to intercarrier interference (ICI) caused by the Doppler spread. This paper discusses ICI suppression analysis using Universal Software Radio Peripheral (USRP) N210 under several Harbor transmission scenarios. Such communication links may contain line of sight (LoS) components in transmission. The channel is thus modeled as the well-known fast time varying path loss model. Furthermore, this paper derives the signal to interference ratio (SIR) and evaluates this parameter for several types of fading and Doppler spread shapes in UGV channels. Additionally, the paper presents a practical method for calculating the spectral efficiency of OFDM systems, with an example for actual implementation in UGV systems. Eventually, the testbed results indicate that the SIR will decrease if the maximum Doppler spread expands. In the Rician channel, it can be seen that the SIR depends on the maximum Doppler speed, the angle of arrival (AoA), and even the Rician element of the LoS component.

INDEX TERMS LTE-A, UAV/UGV, OFDM, ICI cancellation.

I. INTRODUCTION

In recent years, applications for unmanned ground vehicles (UGVs) in transport, public safety and many other commercial sectors have attracted both academic researchers and industry [1]. The most important factor in designing networks for unmanned ground systems (UGSS) is the link distance, which ranges from a few hundred meters to several kilometers [2]. The second factor is a high-speed communication rate even when the user movement is highly rapid [3]. Such factors lead to the choice of operating frequency range, which is currently biased toward the L or C bands [4]. These requirements are also suitable for integration with LTE-A or

5G mobile networks [5], [6]. Qualcomm is testing UAV/UGV for current LTE and 5G mobile applications in different network topologies supporting different IEEE 802.11x protocols.

The standards are developed on the IEEE 802.11 and IEEE 802.16 in the unlicensed band, such as the 5.8 GHz band [7]. There are two significant properties in this type of system. The first is the high Doppler spread, possibly due to the very high-speed of the UGVs, and the second is the appearance of line-of-sight (LoS) components due to low-to-medium-distance transmission [8]. The Wireless Access in Vehicular Environments (WAVE) standard (draft) [9], known as WLAN IEEE 802.11p, has chosen OFDM for the modulation scheme. The OFDM possesses several good wireless communications channel properties such as immunity to the multipath effect, saving bandwidth, and flexibility in

The associate editor coordinating the review of this manuscript and approving it for publication was Muhammad Imran.

spectrum shaping [10], [11]. However, because the subcarriers overlap orthogonally, the OFDM signal is sensitive to the offset frequency caused by the Doppler spread. If the subcarrier orthogonality is destroyed, ICI is introduced, and system performance is degraded [12].

A. RELATED WORK

There has been extensive research on the effect of ICI on OFDM systems in ground vehicle communications with the Rayleigh fading channel only. In [13], the effect of ICI on an OFDM system with application in a digital video broadcast (DVB) is investigated. The ICI is proportional to the number of subcarriers and has a great impact on the DVB signal where many subcarriers are used [14]. An analysis of OFDM signal orthogonality loss caused by Doppler spread is presented in [15]. In [16] and [17], ICI is derived in the time domain for the classic U-shaped Doppler spread model. In [16], the effect of a set carrier frequency due to misalignment of transmitter and receiver oscillators is further considered. In [17], the lower, upper and universal bounds for the ICI power are derived. The results for three Doppler models are presented, namely: two-path, round and classic U-shape via a frequency domain approach. The same accession was used for the Rayleigh fading in [18]. For the classical Doppler shape, the estimation methods are proposed for Rayleigh fading in [17] and Rician fading in [19]. The effect of ICI caused by a classic U-shape Doppler spread on an OFDM signal is analyzed and suppressed by an equalizer in [17], [20], [21]. As the channels for UGV systems are fast time varying with an LoS component characterized by selective Rician fading, their effect on OFDM systems should be reconsidered [22]. In addition, other Doppler shape analysis, for example in [23], is considered under an unrealistic assumption that is uniform AoA approach. In particular, the location of moving scatterers (cars, transit/container, users) as well as roadside scatterers can significantly affect to the measured Doppler shapes [24]. Moreover, in the studies mentioned above, there is still a lack of ICI analysis in OFDM systems for Rician fading channels with different Doppler shapes.

Numerous studies have been done to validate ICI cancellation techniques on Radio Defined Software (SDR). A number of approaches have been widely mentioned in the literature related to SDR research, such as Labview and MATLAB. However, the free software development framework GNU and the Universal Software Radio Peripheral (USRP) are the most popular low-cost but efficient implementations used in SDR systems [25], [26]. The problem of channel estimation is performed on USRP at 300 MHz in [27]. To evaluate the performance of power signal interference cancellation an experiment using USRP N200 with USRP hardware driver (UHD) has been investigated with 10-MHz signal bandwidth in [28]. The author in [29] investigates PSK modulation schemes for various ICI cancellation techniques in LTE transmission scenarios. However, the author does not consider the impact of roadside scatterers (RSS) model,

which leads to different Doppler power spectral density shapes. In [30], the authors have considered a set of delay channel models on the real-time channel emulator and analyzed packet error probabilities using the SDR based on the usual Jakes Doppler model at 5.9 GHz.

B. MOTIVATIONS AND CONTRIBUTIONS

The first motivation of this paper is to analyze the effect of ICI on OFDM systems over both Rayleigh and Rician fading channel with several types of fading and Doppler spread shape. In addition, the closed-form of SIR is derived to predict the SIR level that can be improved in several fading channels as well as several different Doppler Shapes. Concerning the problem of implementing ICI cancellation methods on Testbed, we use real time fading channels instead of taking aforementioned Doppler spread models, which cannot be reproduced in an actual transmission environment. By utilizing the USRP N210 under several Harbor transmission scenarios under either LoS or Non-LoS channels, this paper investigates the ICI suppression analysis in an extensive framework. Our main contributions are briefly summarized as follows:

- We analyze the effects of ICI in the OFDM systems over both Rayleigh and Rician fading channels with four Doppler spread models: two-path, at (uniform), round and classic U-shape. Here, the major factors that affects to V2V and V2I channels as well as their main characteristics are described in detail.
- We derive formulas of SIR for each type of fading and Doppler spread via the time domain approach. Since then, it is possible to predict the extent to which SIR can be improved. In the Rayleigh and Rician fading channels, the SIR decrease if the maximum Doppler spread increases. In wireless communication, the LoS component often improves the quality of the link. However, we shall show that the orthogonality of sub-carriers is destroyed, the quality of the link decreases with the Rician factor in some cases, depending on the angle of arrival of the LoS component.
- In the context of V2V and V2I communications we deploy the different ICI cancellation technologies in a testbed platform based on key parameters of the IEEE 802.11p and conduct several tests to evaluate their spectral efficiency enhancement performance. Instead of taking four aforementioned Doppler spread models, which cannot be reproduced in an actual transmission environment, we use real time fading channels emulated for V2V and V2I communication scenarios in Harbor. And then we summarize and evaluate its relevance in dealing with the time and frequency selectivity of the Harbor UGV channels.
- Both analytical and numerical results unveil interesting observations: The SIR decreases if the maximum Doppler spread increases. The LoS component often improves the link performance. However, the

TABLE 1. Main notations used in this paper.

Notation	Meaning
\otimes	Circular convolution
f_d	Maximum Doppler frequency,
\mathcal{F}^{-1}	Inverse Fourier transform
ρ	Weighted average power in each path
$E[\cdot]$	Expectation of a random variable
$\Re[\cdot]$	Real part of a complex number
δ	Dirac delta function
J_0	Zero-th Bessel function of the first kind
J_1	First Bessel function of the first kind

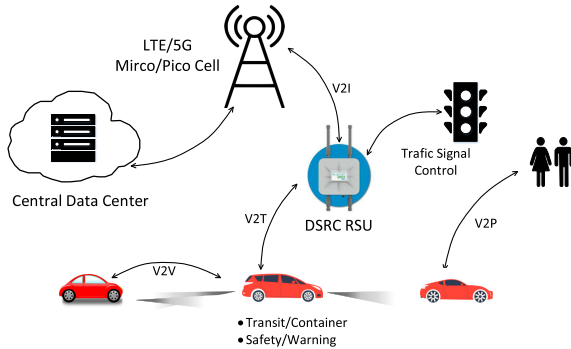


FIGURE 1. Vehicle to infrastructure communication model considered in this paper.

orthogonality of subcarriers is destroyed, and the quality of the link decreases with the Rician factor in some cases.

C. PAPER'S ORGANIZATION

The remaining of this paper is organized as follows: Section II describes the Doppler spread over both Rayleigh and Rician fading channels with four models: two-path, uniform, round and classic U-shape. In Section III, we describe the effects of ICI on OFDM-based UGV systems. After that, we analyze spectral efficiency improvement in different Harbor transmission scenarios in Section IV. We demonstrate the test-bed implementation and show the numerical results in Section V. The main conclusions are given in Section VI. Finally, the main notations used in this paper are presented in Table 1.

II. DOPPLER SPREAD MODELS

A. VEHICLE TO INFRASTRUCTURE CHANNELS

We consider the vehicle to infrastructure communication models as illustrated in Fig. 1. The multipath fading channel can be represented by a tap-delay line model, where each tap is a Rayleigh or Rice random process. Due to vehicle motion, a Doppler spread in the frequency domain is introduced. The power spectral densities and their corresponding autocorrelations for several Doppler spread shapes are listed below. They are pairs of the Fourier transform [31].

1) Two-path model

$$P_T(f) = \rho \cdot \delta(f + f_d) + (1 - \rho) \cdot \delta(f - f_d) \quad (1)$$

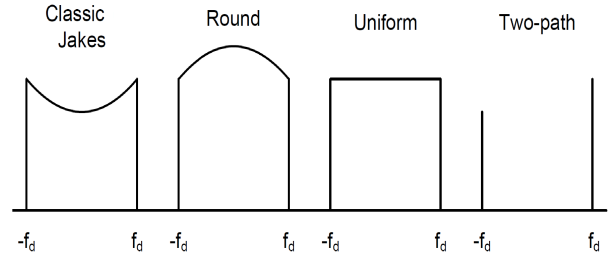


FIGURE 2. Spectral shape of several Doppler spreads.

$$R_T(\tau) = \rho e^{-j2\pi f_d \tau} + (1 - \rho) e^{j2\pi f_d \tau} \quad (2)$$

2) Classic Jakes model

$$P_J(f) = \begin{cases} \frac{1}{\pi f_d} \frac{1}{\sqrt{1 - \left(\frac{f}{f_d}\right)^2}}, & |f| < f_d \\ 0, & \text{otherwise} \end{cases} \quad (3)$$

$$R_J(\tau) = J_0(2\pi f_d \tau) \quad (4)$$

3) Uniform shape model

$$P_U(f) = \begin{cases} \frac{1}{2f_d}, & |f| < f_d \\ 0, & \text{otherwise} \end{cases} \quad (5)$$

$$R_U(\tau) = \text{sinc}(f_d \tau) \quad (6)$$

4) Round shape model

$$P_R(f) = \begin{cases} \sqrt{1 - \left(\frac{f}{f_d}\right)^2}, & |f| < f_d \\ 0, & \text{otherwise} \end{cases} \quad (7)$$

$$R_R(\tau) = \frac{J_1(2\pi f_d \tau)}{2\pi f_d \tau} \quad (8)$$

In all the above equations, $P(f)$ is the power spectral density (PSD) of the signal, and the autocorrelation function (ACF) is denoted by $R(\tau)$.

In the Rician fading channel, the ratio of specular to scattered power is characterized by the Rician factor K , and the angle of arrival (AoA) of the specular component θ_0 . The ACF of the Doppler spreads for two Rayleigh fading channel models are denoted by $R^Y(\tau)$ and $R^I(\tau)$, respectively. Then $R^Y(\tau)$ and $R^I(\tau)$ are related by [32]

$$R^I(\tau) = \frac{K}{1 + K} e^{j2\pi f_d \tau \cos \theta_0} + \frac{1}{1 + K} R^Y(\tau). \quad (9)$$

When $K = 0$, Rician fading reduces to the Rayleigh fading.

B. VEHICLE-TO-VEHICLE CHANNELS

In vehicle to vehicle channels, based on a traditional double-ring scattering model, Akki et al. have shown that the autocorrelation function of the time domain received signal of Rayleigh fading is [33]

$$R_A(\tau) = J_0(2\pi f_1 \tau) J_0(2\pi f_2 \tau), \quad (10)$$

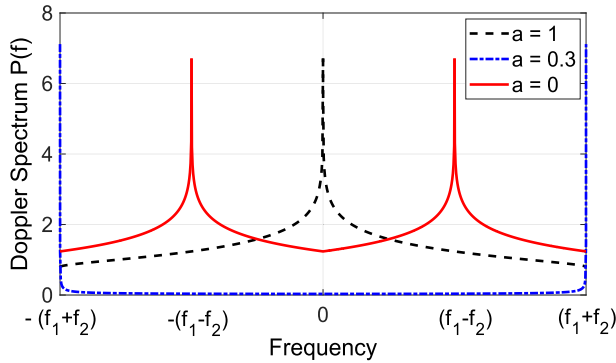


FIGURE 3. Spectral shape of vehicle to vehicle channel with different Doppler shifts.

where f_1 and f_2 are the maximum Doppler frequencies caused by vehicles 1 and 2, respectively. If we assume that $a = f_2/f_1$, and $0 \leq a \leq 1$, Eq. 10 can be rewritten as

$$R_A(\tau) = J_0(2\pi f_1 \tau) J_0(2\pi a f_1 \tau). \quad (11)$$

In the frequency domain, the Doppler spectrum of Akki's model is derived using a Fourier transform on the autocorrelation function in Eq. (10) to give [33]

$$P_A(f) = \frac{1}{\pi^2 f_1 \sqrt{a}} \Re \left[K \left(\frac{1+a}{2\sqrt{a}} \sqrt{1 - \left(\frac{f}{(1+a)f_1} \right)^2} \right) \right], \quad (12)$$

where $K(\cdot)$ denotes the complete elliptic integral of the first kind. The Doppler spectra of vehicle-to-vehicle channel Rayleigh fading channels are illustrated in Fig. 3 when $a = 0, 0.3$ and 1 , respectively. The spectrum is limited in frequency band $[-(f_1 + f_2) \quad (f_1 + f_2)]$ and reaches maximum at frequency $[-(f_1 - f_2)$ and $(f_1 - f_2)]$. When $a = 0$, the spectrum is identical to the classical Jakes model.

It is valuable to emphasize that we consider the Dedicated short-range communications (DSRC) standard model based on 802.11p with short range communication link for the typical Harbor transmission. The short range communication link may contain line of sight (LoS) component in transmission. In this situation the channel is modeled as fast time varying Rician fading channel. So the K-factor and the angle of arrival (AoA) play an important role to improve the system performance. In the V2I channel, the vehicle moving with velocity v causes a maximum Doppler shift f_d and the effect of the LoS component is modeled as the first term in Eq. (9). In this term, the angle of arrival θ_0 is the angle between velocity vector \bar{v} and the reference line connecting the transmitter and receiver. If both transceivers are moving with velocities \bar{v}_1 and \bar{v}_2 respectively, we assume that the receiver velocity is set to zero. The relative motion of the transmitter to receiver is the addition of two vector \bar{v}_1 and $-\bar{v}_2$, and the LoS component effect is the one word of these two velocity vectors.

Take note that the velocity vector $-\bar{v}_2$ has the same length as \bar{v}_2 with reference angle $(\pi - \theta_2)$. The equivalent maximum Doppler spread and angle of arrival are represented in Fig. 4

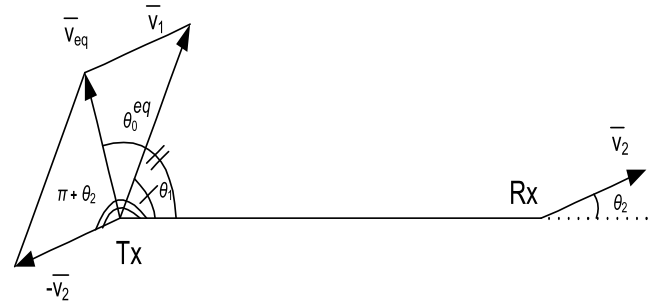


FIGURE 4. Equivalent velocity composed by moving of both transmitter and receiver.

and calculated in Eqs. (13) and (14), respectively

$$f_d^{eq} = \sqrt{f_1^2 + f_2^2 + 2f_1 f_2 \cos(\theta_1 - (\pi - \theta_2))} \\ = \sqrt{f_1^2 + f_2^2 - 2f_1 f_2 \cos(\theta_1 - \theta_2)}, \quad (13)$$

$$\theta_0^{eq} = \tan^{-1} \left(\frac{f_1 \sin \theta_1 + f_2 \sin(\pi - \theta_2)}{f_1 \cos \theta_1 + f_2 \cos(\pi - \theta_2)} \right), \\ = \tan^{-1} \left(\frac{f_1 \sin \theta_1 + f_2 \sin \theta_2}{f_1 \cos \theta_1 - f_2 \cos \theta_2} \right), \quad (14)$$

where θ_1 and θ_2 are the angles between the velocity vectors \bar{v}_1, \bar{v}_2 and the reference line, while the maximum Doppler spreads caused by \bar{v}_1 and \bar{v}_2 are f_1 and f_2 , respectively.

By using the equivalent maximum Doppler shift and angle of arrival, we can reuse the model of the V2V Rician fading channel autocorrelation function of V2V Rician fading channel in Eq. (9).

III. EFFECTS OF ICI ON UGV USING OFDM SYSTEMS

In OFDM systems, the IFFT uses N transmitted data $\{X(k)\}_{k=0}^{N-1}$ at the k th subcarrier, to produce the corresponding N modulated signals in the time domain. The equivalent base-band OFDM signal is [34]

$$x(n) = \frac{1}{\sqrt{N}} \sum_{k=0}^{N-1} X(k) e^{j \frac{2\pi n k}{N}}, \quad n = -N_g, \dots, N-1, \quad (15)$$

where N_g denotes the cyclic prefix length. Due to multipath fading, AWGN noise, and phase noise, the received signal can be written as

$$\hat{x}(n) = \left[x(n) \otimes \mathcal{F}^{-1}(H(k)) \right] + w(n), \quad (16)$$

where $H(k)$ is the channel impulse response (CIR) in the frequency domain. It can also be considered as channel gain on the k th subcarrier., whereas $w(n)$ is the AWGN noise with zero mean and variance σ^2 . After FFT, the demodulated data on the k th sub-carrier is given by

$$\hat{X}[k] = \frac{1}{\sqrt{N}} \sum_{n=0}^{N-1} r[n] e^{-j \frac{2\pi n k}{N}} \quad k = 0, \dots, N-1. \quad (17)$$

Replacing Eqs. (15) and (16) into (17), we have

$$\hat{X}[k] = S[k] + I[k] + W[k], \quad (18)$$

$$\begin{aligned}
 \text{SIR} &= \frac{P_S}{P_I} = \frac{\sum_{p=1-N}^{N-1} (N - |p|) R^I [pT]}{\sum_{m=0, m \neq k}^{N-1} \sum_{p=1-N}^{N-1} (N - |p|) R^I [pT] e^{j\frac{2\pi(m-k)}{N} p}} \\
 &= \frac{\sum_{p=1-N}^{N-1} (N - |p|) (K e^{j2\pi f_d p T \cos \theta_0} + R^Y [pT])}{\sum_{m=0, m \neq k}^{N-1} \sum_{p=1-N}^{N-1} (N - |p|) (K e^{j2\pi f_d p T \cos \theta_0} + R^Y [pT]) e^{j\frac{2\pi(m-k)}{N} p}} \\
 &= \frac{K \times \sum_{p=1-N}^{N-1} (N - |p|) e^{j2\pi f_d p T \cos \theta_0} + \sum_{p=1-N}^{N-1} (N - |p|) R^Y [pT]}{K \times \sum_{m=0, m \neq k}^{N-1} \sum_{p=1-N}^{N-1} (N - |p|) e^{j2\pi (f_d T \cos \theta_0 + \frac{m-k}{N}) p} + \sum_{m=0, m \neq k}^{N-1} \sum_{p=1-N}^{N-1} (N - |p|) R^Y [pT] e^{j\frac{2\pi(m-k)}{N} p}}. \quad (23)
 \end{aligned}$$

where $S[k] = \frac{1}{N} \sum_{n=0}^{N-1} H[n, k] X[k]$ is the desired signal, $I[k] = \frac{1}{N} \sum_{m=0, m \neq k}^{N-1} \sum_{n=0}^{N-1} H[n, m] e^{j\frac{2\pi(m-k)n}{N}} X[m]$ is the interference signal, and $W[k] = \frac{1}{\sqrt{N}} \sum_{n=0}^{N-1} w[n] e^{-j\frac{2\pi nk}{N}}$ is the Fourier transform of the Gaussian noise samples $w[n]$.

We define the power of the desired and interference signal at the k th subcarrier as $P_S = E[|S[k]|^2]$ and $P_I = E[|I[k]|^2]$, respectively. We first calculate P_I as follows

$$\begin{aligned}
 P_I &= E[|I[k]|^2] \\
 &= \frac{1}{N^2} E \left[\left| \sum_{\substack{m=0 \\ m \neq k}}^{N-1} \sum_{n=0}^{N-1} H[n, m] e^{j\frac{2\pi(m-k)n}{N}} X[m] \right|^2 \right]. \quad (19)
 \end{aligned}$$

Without losing objectivity, we can assume that the Fourier transform of the CIR are independent at different frequencies, i.e., $E[H(n_1, m_1) H^*(n_2, m_2)] = R(n_1 - n_2) \delta(m_1 - m_2)$. Likewise, we can assume that data signals at different subcarriers is uncorrelated and has unit power i.e., $E[X(m_1) X^*(m_2)] = \delta(m_1 - m_2)$. Since then, we rewrite the interference power as follows

$$P_I = \frac{1}{N^2} \sum_{\substack{m=0 \\ m \neq k}}^{N-1} \sum_{n_1=0}^{N-1} \sum_{n_2=0}^{N-1} R((n_1 - n_2)T) e^{j\frac{2\pi(m-k)(n_1 - n_2)}{N}}, \quad (20)$$

Following [35], Eq. (20) can be rewritten as

$$P_I = \frac{1}{N^2} \sum_{\substack{m=0 \\ m \neq k}}^{N-1} \sum_{p=1-N}^{N-1} (N - |p|) R(pT) e^{j\frac{2\pi(m-k)}{N} p} \quad (21)$$

Similar argument as made in Eq. (21), we have the signal power as follows

$$P_S = \frac{1}{N^2} \sum_{p=1-N}^{N-1} (N - |p|) R(pT). \quad (22)$$

Substituting the ACF of the Doppler spread spectral shapes into (21) and (22), we determine the SIR for each case.

Theorem 1: The SIR for the Rician fading channel is given in (23), as shown at the top of this page.

Corollary 1: The SIR is a periodical function of angle of arrival θ_0 with period of π .

Proof: Let us consider the SIR for Rician fading channel as a function of angle of arrival θ_0 as given in (23). The two parts relate to variable θ_0 as

$$\begin{aligned}
 g(\theta_0) &= \sum_{p=1-N}^{N-1} (N - |p|) e^{j\mu_d \cos \theta_0} \\
 h(\theta_0) &= \sum_{\substack{m=0 \\ m \neq k}}^{N-1} \sum_{p=1-N}^{N-1} (N - |p|) e^{j2\pi (f_d T \cos \theta_0 + \frac{m-k}{N}) p}. \quad (24)
 \end{aligned}$$

Applying the Lemma in Appendix, the summation can be written by

$$g(\theta_0) = \frac{\sin^2(N\pi f_d T \cos \theta_0)}{\sin^2(\pi f_d T \cos \theta_0)}, \quad (25)$$

$$h(\theta_0) = N^2 - \frac{\sin^2(N\pi f_d T \cos \theta_0)}{\sin^2(\pi f_d T \cos \theta_0)}. \quad (26)$$

Let us consider these functions shifted by a factor π

$$\begin{aligned}
 g(\theta_0 + \pi) &= \frac{\sin^2(N\pi f_d T \cos(\theta_0 + \pi))}{\sin^2(\pi f_d T \cos(\theta_0 + \pi))} \\
 &= \frac{\sin^2(-N\pi f_d T \cos \theta_0)}{\sin^2(-\pi f_d T \cos \theta_0)} \\
 &= \frac{\sin^2(N\pi f_d T \cos \theta_0)}{\sin^2(\pi f_d T \cos \theta_0)} = g(\theta_0), \quad (27)
 \end{aligned}$$

$$\begin{aligned}
 h(\theta_0 + \pi) &= N^2 - \frac{\sin^2(N\pi f_d T \cos(\theta_0 + \pi))}{\sin^2(\pi f_d T \cos(\theta_0 + \pi))} \\
 &= N^2 - \frac{\sin^2(-N\pi f_d T \cos \theta_0)}{\sin^2(-\pi f_d T \cos \theta_0)} \\
 &= N^2 - \frac{\sin^2(N\pi f_d T \cos \theta_0)}{\sin^2(\pi f_d T \cos \theta_0)} = h(\theta_0). \quad (28)
 \end{aligned}$$

Then, we have the following relationship

$$f(\theta_0 + \pi) = f(\theta_0). \quad (29)$$

At this point, we notice that SIR is a periodical function of θ_0 with period π and therefore **Corollary 1** has been proven. ■

Corollary 2: The SIR is a monotonous function (either increasing or decreasing) of Rician factor K .

Proof: The SIR is a function of K as

$$\text{SIR} = \frac{aK + b}{cK + d}. \quad (30)$$

It is easy to see that if $K = 0$ then $SIR = c/d$, if $K \rightarrow \infty$, the SIR approaches a/b . The first-order derivative of SIR over the Rician factor variable K is

$$SIR' = \frac{ad - bc}{(cK + d)^2}. \quad (31)$$

Because this derivative is either positive or negative depending on parameters f_d , T , and θ_0 , the SIR is a monotone function of K . ■

Now, we consider the various aforementioned Doppler spread shapes for both Rayleigh and Rician fading channels. The SIR in all the discussed cases reads as $SIR = \frac{P_S}{P_I}$. Therefore, we will only present the expressions for relevant P_S and P_I .

IV. ENERGY AND SPECTRAL EFFICIENCY ANALYSIS

This section studies the influence of transmission power levels to the ergodic spectral efficiency of our considered network. We first reformulate the base-band OFDM signal in (15) as

$$x[n] = \frac{\sqrt{\rho}}{\sqrt{N}} \sum_{k=0}^{N-1} X[k] e^{j\frac{2\pi nk}{N}}, \quad n = 0, \dots, N - 1, \quad (32)$$

where $\rho > 0$ is the transmission power level allocated to each OFDM symbol and $|X[k]|^2 = 1$. After that, the received signal is given by

$$r[n] = \frac{\sqrt{\rho}}{\sqrt{N}} \sum_{k=0}^{N-1} H[n, k] X[k] e^{j\frac{2\pi nk}{N}} + w[n], \quad n = 0, \dots, N - 1. \quad (33)$$

Here, we assume that noise symbols $w[n]$ follows a complex Gaussian distribution with zero mean and variance σ^2 . Consequently, the second moment of Gaussian noise at the receiver is computed as

$$P_N = E[|W[k]|^2] = \sigma^2. \quad (34)$$

Following similar steps to compute the powers of the desired signal and mutual interference, then using the capacity bounding method in [36], [37], we obtain the ergodic spectral efficiency measured in b/s/Hz as given in (35), as shown at the bottom of this page.

In (35), the fraction inside the logarithm represents the signal-to-interference and noise ratio, in which the numerator is the power of the desired signal. Meanwhile, the first part of the denominator is mutual interference caused by the Fourier transform process. The last part is Gaussian noise intensity. We further introduce the energy efficiency of our considered

process as

$$EE = \frac{R}{\rho + \hat{\rho}}, \quad (36)$$

where $\hat{\rho}$ is the hardware circuit used for the Fourier computation. At this point, we emphasize that both (35) and (36) allow us to study the effects of power allocation in UGV systems using the OFDM technique.

V. TEST FIELD AND NUMERICAL RESULTS

A. EXPERIMENTAL SETUP

The measurement positions considered in this paper include the rich diversity of practical scenarios of communication in Harbor. The test network, including (i) on-board units (OBUs) installed in harbor vehicles, (ii) roadside units built on the main road, and the control system to evaluate network performance. Our proposed UGV prototype was tested in an outdoor university campus environment, the transceivers are placed on cars a few hundred meters apart, so noise and signal attenuation play a major role. The measurement positions considered in this paper are consistent with the rich variety of actual scenarios in the harbor area.

This experiment was conducted on two main platform parts. The first, called GNU Radio, is responsible for signal processing and running in a host PC, whereas the second is USRP N210 paired with Ettus daughter-boards XCVR2450, which serve as the RF front-end at 5.9 GHz. Because the power output of the XCVR2450 is 100 mW, a power amplifier is adopted to archive a TX power level of 23 dBm. Finally, there is the Omni 5 dBi Antenna.

The specific parameters of the WAVE IEEE 802.11p are used to illustrate the above analysis. In the WAVE standard, the OFDM system is employed. The typical parameters are described in Table 2.

TABLE 2. Parameters of IEEE 802.11p.

Parameters	Values
Carrier frequency	5.9 GHz
Bandwidth	10 MHz
Symbol duration	8 μ s
Guard Time	1.6 μ s
Number of FFT point	64
Number of subcarrier	52
Number of useful subcarrier	48
Frequency spacing	0.15625 MHz

We conducted the experiment with different ICI cancellation methods enumerated as follows:

- 1) $(a_i, -a_i)$ are mapped to subcarriers with indices of $2i$ and $2i + 1$ [38]. This is the simplest method, since the

$$R = \log_2 \left(1 + \frac{\rho \sum_{p=1-N}^{N-1} (N - |p|) R[pT]}{\rho \sum_{m=0, m \neq k}^{N-1} \sum_{p=1-N}^{N-1} (N - |p|) R(pT) e^{j\frac{2\pi(m-k)p}{N}} + N^2 \sigma^2} \right). \quad (35)$$

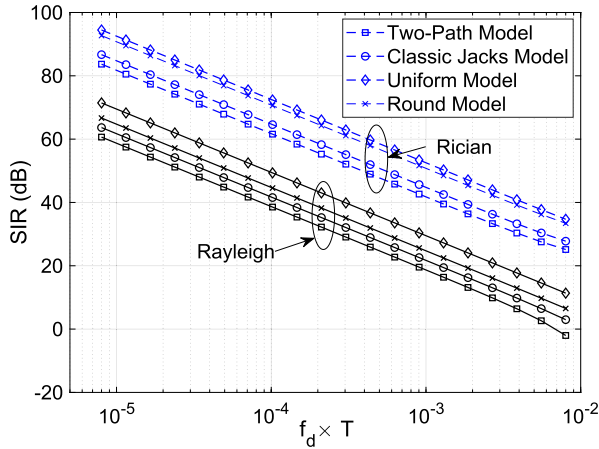


FIGURE 5. SIR for V2I communications.

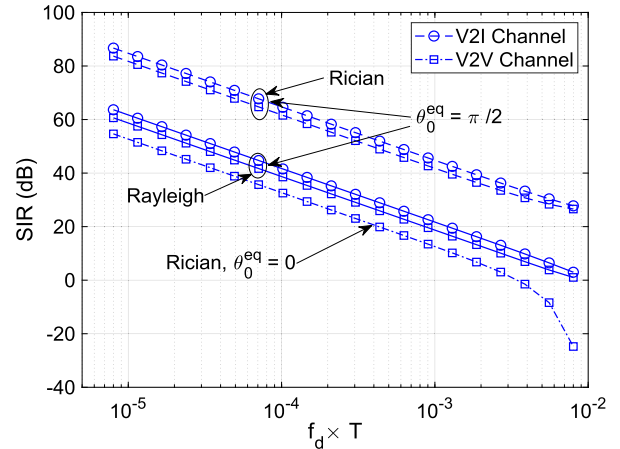


FIGURE 6. SIR for V2I and V2V communications.

original signals are derived directly from the summation of subcarrier signal pairs. This ICI cancellation method is Adjacent Cancellation (AC).

- 2) $(a_i, -a_i^*)$ are mapped to subcarriers with indices of $2i$ and $2i+1$ [39]. This scheme is similar to the AC method but different coefficients are used. Thus, the demodulation process is also different from the AC method. In another words, a different decision variable from the difference of adjacent subcarriers is considered to recover the original signal. This ICI cancellation method is the Conjugate method (CC).
- 3) $(a_i, -a_i, -a_i^*, a_i^*)$ are mapped to subcarriers with indices of from $2i$ to $2i + 3$ [40]. This is a combination of two previous methods that uses both weights of -1 and $e^{-j\frac{\pi}{2}}$. Hence, four sequential subcarriers will carry a single useful symbol with particular coefficients. This ICI cancellation method is the Improved Conjugate method (IC).

B. RESULTS AND DISCUSSION

It is clear that when the vehicle speed increases, it will lead to an increasing of maximum Doppler spread and as a result, the SIR drops. Then the SINR at the input of the receiver device is limited by the dropped SIR value regardless for any SNR average. This is shown in the equation:

$$\frac{1}{\text{SINR}} = \frac{1}{\text{SIR}} + \frac{1}{\text{SNR}}. \quad (37)$$

As a result, the BER will gradually reach an error floor level. In specific cases, if UGVs velocity is $v = 300$ km/h at $f_c = 5.9$ GHz and the speed of light is denoted by $c = 3 \times 10^8$ m/s, We determine f_d as follows

$$f_d = \frac{vf_c}{c} = \frac{300 \times 10^3 \times 5.9 \times 10^9}{3600 \times 3 \times 10^8} \approx 1638 \text{ Hz} \quad (38)$$

Fig. 5 shows the SIR for the Rayleigh and Rician fading channel given in (23) with the LoS component AoA being $\theta_0 = \pi/2$ and the Rician factor $K = 2$ dB, in which solid curves are used to describe the Rayleigh channel and dash

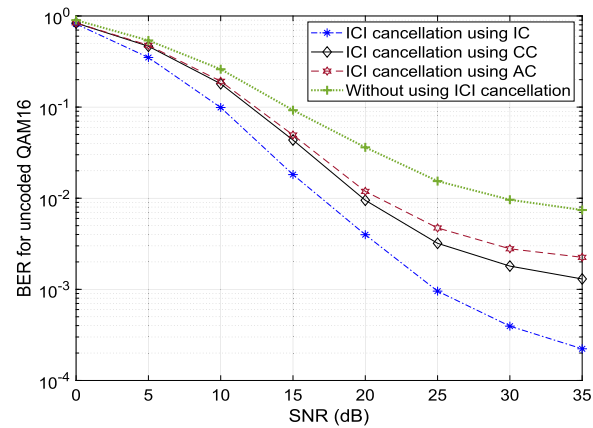


FIGURE 7. BER performance at $f_{D\max} = 163.8$ Hz corresponds to a typical UGV speed in the Harbor of 30km/h with three different ICI cancellation methods.

curves depicting the Rician channel. In this case, the specular component improves the system SIR significantly, e.g. the SIR for the two-path model improves about 25 dB. This is consistent with the theory that LoS component plays the most important role in ensuring transmission quality.

The OFDM symbol duration of 802.11p standard is $T_s = 8\mu\text{s}$, so $f_d T \approx 1.31 \times 10^{-2}$. For this case, the SIR of Two-path, Classic Jakes, Uniform and Round models are -2 ; 3 ; 6.5 and 11.5 dB, respectively. If in a traffic environment, for example in a harbor or urban area, the UGVs velocity slows to $v = 30$ km/h, the maximum Doppler frequency is $f_d \approx 163.8$ Hz, correspondingly. The SIR for four aforementioned Doppler spectrum models increases than to 19; 22; 25 and 29 dB, respectively. The fading with the two-path model of the Doppler spread causes the most severe ICI in the OFDM signal. At the same level of maximum Doppler frequency, the SIR with two-path fading is 10 dB worse than uniform fading.

Fig. 7 and Fig. 8 illustrate the BER performance at the receiver side of the ground aerial vehicle system, with the vehicle speed being 30 km/h, with the use of three different

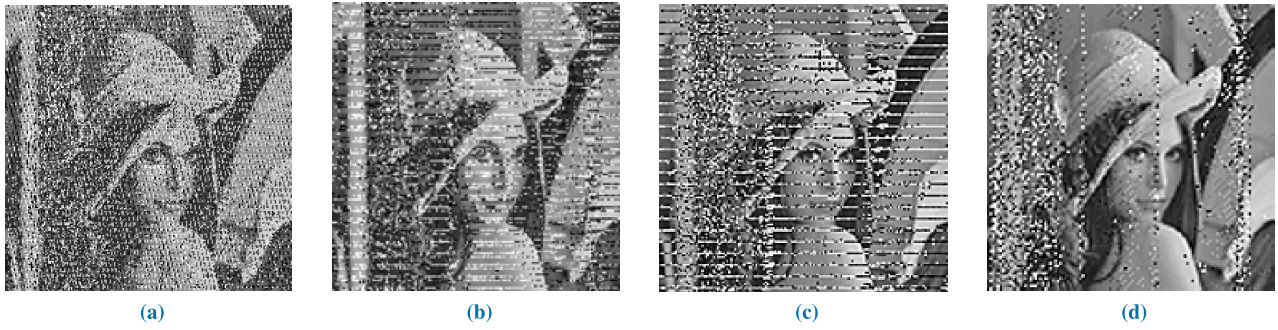


FIGURE 8. System performance with $f_{Dmax} = 163.8$ Hz corresponds to a typical UGV speed in the Harbor of 30km/h. (a) Without ICI Cancellation BER = 22.3%, (b) AC method, BER = 15.6%, (c) CC method, BER = 14.6%, (d) IC method, BER = 9.8%.

an ICI cancellation schemes, and a case where ICI cancellation method is not used. As we mentioned in the introduction that it is not feasible to reproduce Doppler’s shapes in the actual transmission environment. So in this part, we do not evaluate the ICI cancellation methods for each Doppler Shape. Instead, the V2V in Harbor communication scenarios were built according to the 802.11p standard, to evaluate the performance of the ICI Cancellation methods evaluated on the USRP N210 Testbed.

Fig. 7 describes BER in theory for uncoded QAM-16 over actual V2V channel. Obviously, the IC method offers the best BER performance, while absence of ICI Cancellation has the worst results. Whereas with the same data rate and spectrum efficiency, the CC method is more efficient than AC.

It is worth noting that in implementing of testbed in practice, it is impossible to measure SIR as well as SINR. Whereas, measuring SNR depends on the zero padding component. So in the results shown in Fig. 8, we do not measure ground noise to calculate BER versus SNR but directly compare the error rate compared to the original image. It can be seen clearly that the image quality when using ICI cancellation methods is much better than without ICI canceling. The results show that the IC method has a much lower BER than other methods. Specifically, IC has BER = 9.8% compared to CC = 14.5%, AC = 15.3%. In the absence of ICI cancellation, BER = 22.3%.

Fig. 6 compares the SIR performance of the classic Jakes model over the V2I channels with the SIR over the V2V channels. The SIR over the V2V Rician fading channel is heavily dependent on the equivalent AoA θ_0^{eq} . Here, when the two vehicles move with the same speed, i.e. $a = 1$, and if the equivalent AoA $\theta_0^{eq} = \pi/2$, the SIR over the Rayleigh and Rician V2V channels degrade approximately 3 dB compared to the V2I channels. However, if the equivalent AoA $\theta_0^{eq} = 0$, the SIR over the Rician V2V channel drops more than 32 dB from its value in the V2I channel.

Let us next consider the SIR for the Rician fading channel with respect to both AoA θ_0 and Rician factor K at the same time at $f_d = 1000$ Hz. The results are shown in Figs. 9 and 10, for the two-path and the uniform Doppler spread models, respectively. For the two-path model, at any given value of

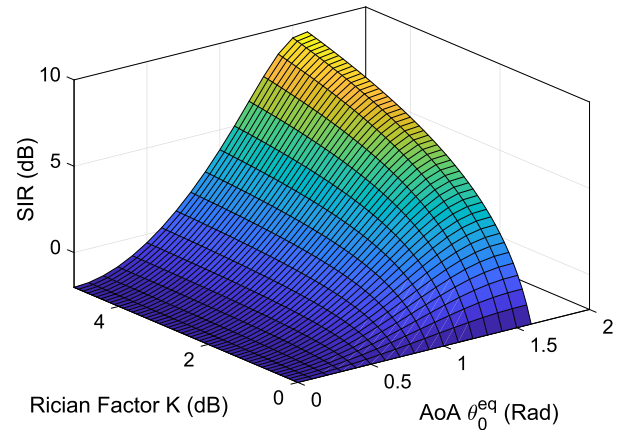


FIGURE 9. SIR versus θ_0 and K for the Rician fading channels of the two-path model.

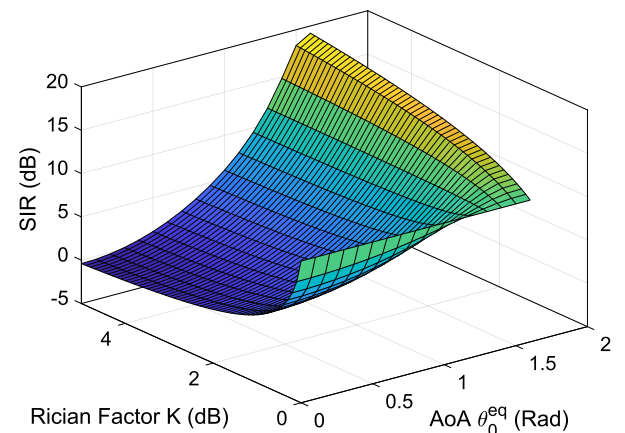


FIGURE 10. SIR versus θ_0 and K for the Rician fading channels of the uniform model.

θ_0 , the SIR increases with the Rician factor K . However, for the uniform model, whether the SIR increases or decreases with K depends on the AoA θ_0 . This means that the LoS component plays either a constructive or destructive role in maintaining the quality of the transmission link. These results are shown details in Fig. 11, where f_d is set to 1000 Hz, while

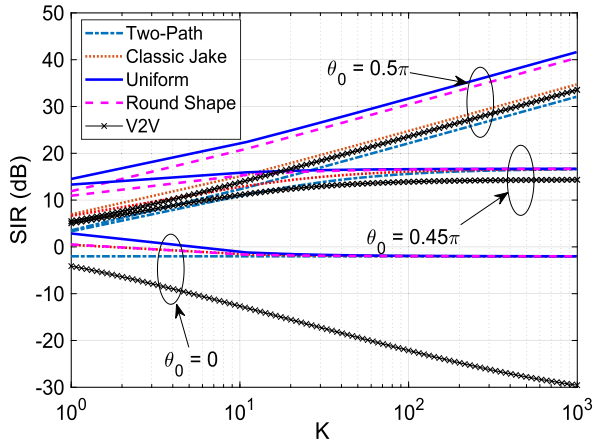


FIGURE 11. SIR versus K for the Rician fading channels.

the AoA of LoS components are varied over $\theta_0 = 0; 0.45\pi$ and 0.5π , respectively.

In Fig. 11, over the various V2I channels, at a given value of θ_0 , The SIR result of the two-path model is the lowest, while the highest SIR is in the uniform model. Especially, in the two-path model, the SIR result is constant unchanged in the case of the AoA $\theta_0 = 0$ and increases as K increases in cases AoA has different values. For the classic Jakes, round and uniform, at $\theta_0 = 0$, if K increases, the SIR drops to a saturation level as Two-path model. It can be concluded that in such a situation, the LoS components have seriously degraded the quality of transmission links. In two cases $\theta_0 = 0.45\pi$ and 0.5π , the SIR increases with K monotonously. This is consistent with the theoretical basis that has been demonstrated at **Corollary 2**. In the V2V communication, at the equivalent AoA $\theta_0^{eq} = 0$, for example two vehicles move far away in opposite directions, the very large degradation of SIR versus K is taken into account. Let θ_0^* denote a critical value of AoA, at which point the SIR for each of the above-mentioned Doppler spread models is constant. This parameter indicates that, if AoA is greater than θ_0^* , then the SIR will increase monotonously with K , and vice versa, if AoA is less than θ_0^* , then the SIR will decrease monotonously with K . The reference value θ_0^* is determined by solving the first derivative equation of SIR for K equals 0. However, this problem is complex and thus usually solved by numerical methods. For example, in the classic Jakes model, if $f_d = 1$ KHz, the reference AoA $\theta_0^* = 0.8313$ rad. Whereas, if $f_d = 100$ Hz $\theta_0^* = 0.7858$ rad.

In Fig. 12, the change of SIR with respect to AoA is shown. In this figure, the maximum Doppler spread is $f_d = 1$ KHz and the Rician factor $K = 10$. It is shown that the SIR is a periodic function of AoA θ_0 with period π . This has been proven on the basis of theory at **Corollary 1**. The SIR reaches its maximum value at $\theta_0 = \pm k\pi/2$ and its minimum value at $\theta_0 = \pm k\pi$ with $k \in N$.

Figs. 13 and 14 illustrate the energy efficiency with different models as a function of the total power consumption

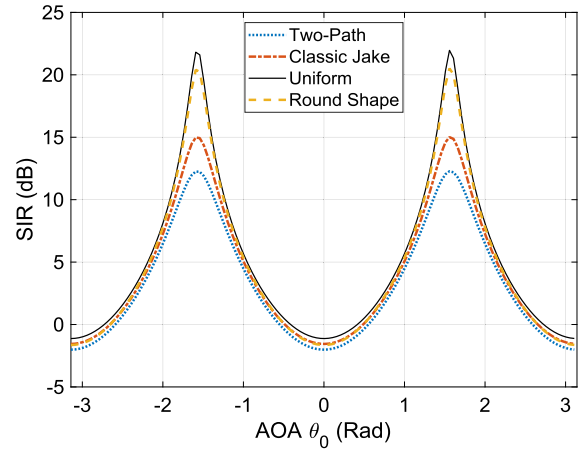


FIGURE 12. SIR versus θ_0 for the Rician fading channels.

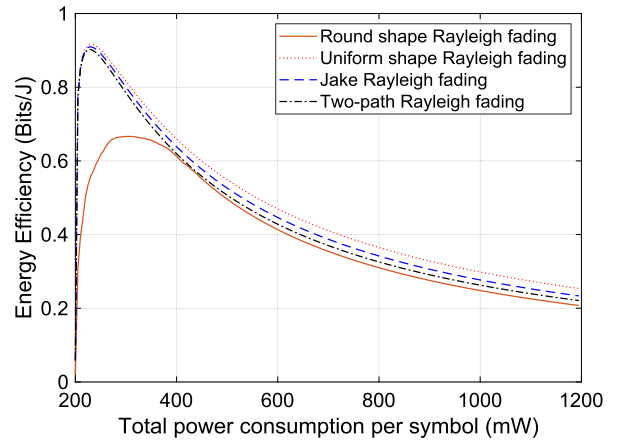


FIGURE 13. Energy efficiency versus total power consumption for Rician channels.

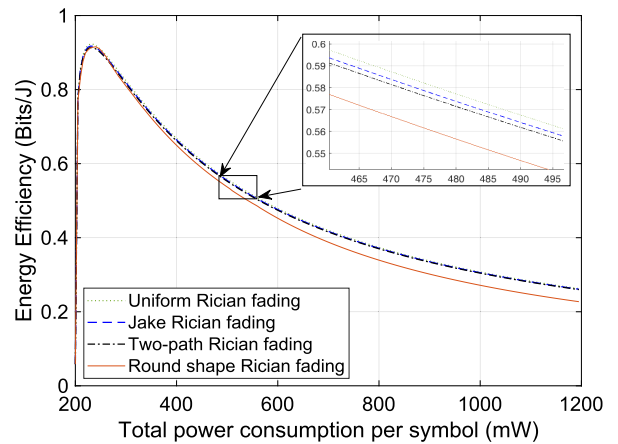


FIGURE 14. Energy efficiency versus total power consumption for Rayleigh channel.

(measured in mW). The channel model is either Rayleigh or Rician fading. We use the hardware power of 200 mW and the transmit power varies from 0 to 1000 mW. At first, increasing the transmit power results in better energy efficiency. The

$$S_1 = \sum_{p=1-N}^{N-1} (N - |p|) e^{j2\pi f_d T p} = \frac{\sin^2(N\pi f_d T)}{\sin^2(\pi f_d T)}, \quad (39)$$

$$S_2 = \sum_{m=0, m \neq k}^{N-1} \sum_{p=1-N}^{N-1} (N - |p|) e^{j2\pi (f_d T + \frac{m-k}{N}) p} = N^2 - \frac{\sin^2(N\pi f_d T)}{\sin^2(\pi f_d T)}. \quad (40)$$

system achieves the peak energy efficiency of 7 Mbits/J if one uses the round shape model for Rayleigh fading, whereas the other models give a significantly higher value of approximately 9 Mbits/J peak energy efficiency. The further increasing power consumption leads to more severe interference, and therefore, energy efficiency is reduced up to approximately 3.5 compared to the peak point if the system consumes 1500 mW for both transmit and hardware power to process each data symbol.

VI. CONCLUSION

The ETSI and IEEE 802.11p standards use OFDM as a modulation scheme for Intelligent Transport System (ITS) applications with unmanned ground vehicles (UGV). However, high vehicle speed causes high Doppler spread, which in turn destroys the orthogonality of subcarriers in OFDM, causing SIR. In short-range communication scenarios, especially applications in Harbor, the LoS component typically exists and the Rician fading channel model applies. This paper investigates ICI suppression methods using Universal Software Radio Peripheral (USRP) N210 under several Harbor transmission scenarios. Such communication links are analyzed for both Rayleigh and Rician channels with several Doppler spread models. Closed-form expressions for the SIR and energy efficiency are derived. The results show that the degree that SIR is degraded depending on the maximum Doppler frequency or vehicle speed. The AoA of the LoS component in the Rician fading channel also affects SIR in an interesting way, specifically, SIR may increase or decrease with the Rician factor K of the specular component, depending on the LoS path AoA. Finally, we reveal the trend of energy efficiency as a function of the total power consumption.

**APPENDIX
USEFUL EQUATIONS**

In this part, we show some results that are frequently used in this paper.

Lemma 1: We have two equalities given in (39) and (40), as shown at the top of this page.

Proof: The first equation (39) can be represented by

$$S_1 = N \sum_{p=1-N}^{N-1} e^{j\mu_d p} - \sum_{p=1-N}^{N-1} |p| e^{j\mu_d p}. \quad (41)$$

Applying (1-342-2) in [41], the first summation is

$$N \sum_{p=1-N}^{N-1} e^{j2\pi f_d T p} = N \frac{\sin((2N - 1)\pi f_d T)}{\sin(\pi f_d T)}, \quad (42)$$

$$\sum_{p=1-N}^{N-1} |p| e^{-j2\pi f_d T p} = 2 \sum_{p=1}^{N-1} p \cos(2\pi f_d T p). \quad (43)$$

Applying (1-352-2) in [41], the second summation can be rewritten as

$$\begin{aligned} & \sum_{p=1-N}^{N-1} |p| e^{j2\pi f_d T p} \\ &= \frac{N \sin((2N - 1)\pi f_d T)}{\sin(\pi f_d T)} - \frac{1 - \cos(2\pi f_d T)}{2 \sin^2(\pi f_d T)} \\ &= N \frac{\sin((2N - 1)\pi f_d T)}{\sin(\pi f_d T)} - \frac{\sin^2(N\pi f_d T)}{\sin^2(\pi f_d T)}. \end{aligned} \quad (44)$$

Replacing these two parts into S_1 , we have

$$\begin{aligned} S_1 &= N \frac{\sin((2N - 1)\pi f_d T)}{\sin(\pi f_d T)} \\ &\quad - \left[N \frac{\sin((2N - 1)\pi f_d T)}{\sin(\pi f_d T)} - \frac{\sin^2(N\pi f_d T)}{\sin^2(\pi f_d T)} \right] \\ &= \frac{\sin^2(N\pi f_d T)}{\sin^2(\pi f_d T)}. \end{aligned} \quad (45)$$

The first equality (39) is proven. We now apply the same analysis of S_1 to S_2 and obtain

$$\begin{aligned} S_2 &= \sum_{\substack{m=0 \\ m \neq k}}^{N-1} \frac{\sin^2(N\pi (f_d T + \frac{m-k}{N}))}{\sin^2(\pi (f_d T + \frac{m-k}{N}))} \\ &= \sin^2(N\pi f_d T) \sum_{\substack{m=0 \\ m \neq k}}^{N-1} \frac{1}{\sin^2(\pi (f_d T + \frac{m-k}{N}))}. \end{aligned} \quad (46)$$

Let us consider the summation part. Applying (4.4.6.9) in [42] and exploiting the fact that function $\text{cosec}^2(x)$ is periodical with period π , the summation can be written as

$$\begin{aligned} & \sum_{m=0, m \neq k}^{N-1} \frac{1}{\sin^2(\pi (f_d T + \frac{m-k}{N}))} \\ &= \sum_{m=0, m \neq k}^{N-1} \text{cosec}^2\left(\pi f_d T + \frac{m-k}{N} \pi\right) \\ &= N^2 \text{cosec}^2(N\pi f_d T) - \text{cosec}^2(\pi f_d T). \end{aligned} \quad (47)$$

The summation S_2 is

$$S_2 = \sin^2(N\pi f_d T) \left(N^2 \operatorname{cosec}^2(N\pi f_d T) - \operatorname{cosec}^2(\pi f_d T) \right) \\ = N^2 - \frac{\sin^2(N\pi f_d T)}{\sin^2(\pi f_d T)}, \quad (48)$$

and therefore the second equality (40) is proven. ■

REFERENCES

- [1] S. Hayat, E. Yanmaz, and R. Muzaffar, "Survey on unmanned aerial vehicle networks for civil applications: A communications viewpoint," *IEEE Commun. Surveys Tuts.*, vol. 18, no. 4, pp. 2624–2661, 4th Quart., 2016.
- [2] R. Jain, F. Templin, and K.-S. Yin, "Wireless datalink for unmanned aircraft systems: Requirements, challenges, and design ideas," in *Proc. Infotech Aerospace*, 2011, p. 1426.
- [3] *Intelligent Transportation Systems (ITS): Vehicular Communication; Basic Set of Applications; Definition*, ETSI, Sophia Antipolis, France, Jan. 2009.
- [4] J. Kakar and V. Marojevic, "Waveform and spectrum management for unmanned aerial systems beyond 2025," in *Proc. IEEE 28th Annu. Int. Symp. Pers., Indoor, Mobile Radio Commun. (PIMRC)*, Oct. 2017, pp. 1–5.
- [5] Y. Zeng, R. Zhang, and T. J. Lim, "Wireless communications with unmanned aerial vehicles: Opportunities and challenges," *IEEE Commun. Mag.*, vol. 54, no. 5, pp. 36–42, May 2016.
- [6] G. Sun, G. O. Boateng, D. Ayepah-Mensah, and G. Liu, "Relational reinforcement learning based autonomous cell activation in cloud-RANs" *IEEE Access*, vol. 7, pp. 63588–63604, 2019.
- [7] Y. Zeng, J. Lyu, and R. Zhang, "Cellular-connected UAV: Potential, challenges, and promising technologies," *IEEE Wireless Commun.*, vol. 26, no. 1, pp. 120–127, Feb. 2018.
- [8] G. N. Wilson, A. Ramirez-Serrano, and Q. Sun, "Vehicle state prediction for outdoor autonomous high-speed off-road UGVs," in *Proc. IEEE Int. Conf. Robot. Autom. (ICRA)*, Seattle, WA, USA, May 2015, pp. 467–472.
- [9] *IEEE Draft Standard for Information Technology – Telecommunications and information exchange between systems – Local and metropolitan area networks – Specific requirements – Part 11: Wireless LAN Medium Access Control (MAC) and Physical Layer (PHY) specifications Amendment 7: Wireless Access in Vehicular Environments*, IEEE Standard P802.11p /D7.0, Nov. 2008.
- [10] V.-D. Nguyen, H. Haas, K. Kyamakya, J. C. Chedjou, T. H. Nguyen, S. Yoon, and H. Choo, "Decentralized dynamic sub-carrier assignment for OFDMA-based adhoc and cellular networks," *IEICE Trans. Commun.*, vol. 92, no. 12, pp. 3753–3764, Dec. 2009.
- [11] E. H. C. Harik, F. Guérin, F. Guinand, B. Brethé, and H. Pelvillain, "UAV-UGV cooperation for objects transportation in an industrial area," in *Proc. IEEE Int. Conf. Ind. Technol. (ICIT)*, Seville, Spain, Mar. 2015, pp. 547–552.
- [12] Q. Han, X. Li, M. Temple, and Z. Wu, "Inter-carrier interference cancellation for wideband OFDM in high speed aerial vehicle communication," in *Proc. Int. Conf. Comput., Netw. Commun. (ICNC)*, Jan. 2013, pp. 23–27.
- [13] V. Vahidi and E. Saberinia, "ICI mitigation for high-speed OFDM communications in high-mobility vehicular channels," in *Information Technology - New Generations*. New York, NY, USA: Springer, 2018, pp. 17–22.
- [14] J.-K. Choi, H. N. Nguyen, T. H. Nguyen, H. Cho, H. K. Choi, and S. G. Park, "A time-domain estimation method of rapidly time-varying channels for OFDM-based LTE-R systems," *Digit. Commun. Netw.*, vol. 5, no. 2, pp. 94–101, May 2018.
- [15] X. Zhang, M. Jia, L. Chen, J. Ma, and J. Qiu, "Filtered-OFDM - Enabler for flexible waveform in the 5th generation cellular networks," in *Proc. IEEE Global Commun. Conf. (GLOBECOM)*, San Diego, CA, USA, Dec. 2015, pp. 1–6.
- [16] Y. Shui F. Li, J. Yu, W. Chen, C. Li, K. Yang, and F. Chang, "Vehicle-to-vehicle radio channel characteristics for congestion scenario in dense urban region at 5.9GHz," Apr. 2018.
- [17] S. Beygi, E. G. Strom, and U. Mitra, "Geometry-based stochastic modeling and estimation of vehicle to vehicle channels," in *Proc. IEEE Int. Conf. Acoust., Speech Signal Process. (ICASSP)*, Florence, Italy, May 2014, pp. 4289–4293.
- [18] I. Capoglu, Y. Li, and A. Swami, "Effect of Doppler spread in OFDM-based UWB systems," *IEEE Trans. Wireless Commun.*, vol. 4, no. 5, pp. 2559–2567, 2005.
- [19] J. Tao, J. Wu, and C. Xiao, "Doppler spread estimation for broadband wireless OFDM systems over Rician fading channels," *Int. J. Wireless Inf. Netw.*, vol. 16, no. 4, pp. 197–208, 2009.
- [20] W. G. Jeon, K. H. Chang, and Y. S. Cho, "An equalization technique for orthogonal frequency-division multiplexing systems in time-variant multipath channels," *IEEE Trans. Commun.*, vol. 47, no. 1, pp. 27–32, Jan. 1999.
- [21] P. Schniter, "Low-complexity equalization of OFDM in doubly selective channels," *IEEE Trans. Signal Process.*, vol. 52, no. 4, pp. 1002–1011, Apr. 2004.
- [22] H. Cho, T. H. Nguyen, H. N. Nguyen, H. K. Choi, J. K. Choi, and S. Ro, "A robust ICI suppression based on an adaptive equalizer for very fast time-varying channels in LTE-R systems," *EURASIP J. Wireless Commun. Netw.*, vol. 1, p. 17, Jan. 2018.
- [23] X. Liang, X. Zhao, S. Li, Q. Wang, and J. Li, "A non-stationary geometry-based scattering model for street vehicle-to-vehicle wideband MIMO channels," in *Proc. IEEE 26th Annu. Int. Symp. Pers., Indoor, Mobile Radio Commun. (PIMRC)*, Sep. 2015, pp. 2239–2243.
- [24] M. I. Ashraf, C. F. Liu, M. Bennis, W. Saad, and C. S. Hong, "Dynamic resource allocation for optimized latency and reliability in vehicular networks," *IEEE Access*, vol. 6, pp. 63843–63858, 2018.
- [25] A. Marwanto, M. A. Sarijari, N. Faisal, S. K. S. Yusof, and R. A. Rashid, "Experimental study of OFDM implementation utilizing GNU radio and USRP—SDR," in *Proc. IEEE 9th Malaysia Int. Conf. Commun. (MICC)*, Dec. 2009, pp. 132–135.
- [26] H. D. Han, H. T. Nguyen, and T. H. Nguyen, "Implementation of an OFDM system based on the TMS320C6416 DSP," in *Proc. Int. Conf. Adv. Technol. Commun.*, Oct. 200, pp. 74–77.
- [27] L. C. Tran, D. T. Nguyen, F. Safaei, and P. J. Vial, "An experimental study of OFDM in software defined radio systems using GNU platform and USRP2 devices," in *Int. Conf. Adv. Technol. Commun.*, Oct. 2014, pp. 657–662.
- [28] K. Yamazaki, Y. Sugiyama, Y. Kawahara, S. Saruwatari, and T. Watanabe, "Interference cancellation for coexisting wireless data and power transmission in the same frequency," in *J. Phys. Conf. Ser.*, vol. 557, Art. no. 012004.
- [29] N. N. Huu, H. Y. Quoc, L. van Pham, T. H. Nguyen, H. Cho, N. van Nguyen, and B. Jeon, "An OFDM System Design with Efficient ICI Cancellation over Embedded LTE-R Channels Based on the USRP Platform," in *Proc. 12th Int. Conf. Ubiquitous Inf. Manage. Commun.*, Jan. 2018, pp. 1–10.
- [30] T. Blazek, M. Ashury, and C. F. Mecklenbräuker, D. Smely, and G. Ghiaasi, "Vehicular channel models: A system level performance analysis of tapped delay line models," in *15th Int. Conf. ITS Telecommun. (ITST)*, pp. 1–8, Aug. 2017.
- [31] J. Dulmage and M. P. Fitz, "Non-Isotropic fading channel model for the highway environment," in *Proc. IEEE 66th Veh. Technol. Conf.*, Baltimore, MD, USA, 2007, pp. 2144–2148.
- [32] C. Xiao, Y. R. Zheng, and N. C. Beaulieu, "Novel sum-of-sinusoids simulation models for Rayleigh and Rician fading channels," *IEEE Trans. Wireless Commun.*, vol. 5, no. 12, pp. 3667–3679, Dec. 2006.
- [33] A. S. Akki and F. Haber, "A statistical model of mobile-to-mobile land communication channel," *IEEE Trans. Veh. Technol.*, vol. 35, no. 1, pp. 2–7, Feb. 1986.
- [34] S. Wu and Y. Bar-Ness, "OFDM systems in the presence of phase noise: Consequences and solutions," *IEEE Trans. Commun.*, vol. 52, no. 11, pp. 1988–1996, Nov. 2004.
- [35] J. Li and M. Kavehrad, "Effects of time selective multipath fading on OFDM systems for broadband mobile applications," *IEEE Commun. Lett.*, vol. 3, no. 12, pp. 332–334, Dec. 1999.
- [36] T. Van Chien and C. Möllén, and E. Björnson, "Large-scale-fading decoding in cellular massive MIMO systems with spatially correlated channels," *IEEE Trans. Commun.*, vol. 67, no. 4, pp. 2746–2762, Apr. 2019.
- [37] T. H. Nguyen, T. K. Nguyen, H. D. Han, and V. D. Nguyen, "Optimal power control and load balancing for uplink cell-free multi-user massive MIMO," *IEEE Access*, vol. 6, pp. 14462–14473, 2018.
- [38] Y. Zhao and S. G. Haggman, "Inter-carrier interference self-cancellation scheme for OFDM mobile communication systems," *IEEE Trans. Commun.*, vol. 49, no. 7, pp. 1185–1191, Jul. 2001.
- [39] H. G. Yeh, Y. K. Chang, and B. Hassibi, "A scheme for cancelling inter-carrier interference using conjugate transmission in multicarrier communication systems," *IEEE Trans. Wireless Commun.*, vol. 6, no. 1, pp. 3–7, Jan. 2007.

- [40] H.-G. Ryu, Y. Li, and J.-S. Park, "An Improved ICI Reduction Method in OFDM Communication System," *IEEE Trans. Broadcast.*, vol. 51, no. 3, pp. 395–400, Sep. 2005.
- [41] I. S. Gradshteyn and I. M. Ryzhik, *Table of Integrals, Series, and Products*. New York, NY, USA: Academic Press, 2007.
- [42] A. P. Prudnikov, Y. A. Brychkov, and O. I. Marichev, *Integrals Series: Elementary functions*, vol. 1. Boca Raton, FL, USA: CRC Press, 1986.



TIEN HOA NGUYEN received the Dip-Ing. degree in electronics and communication engineering from Hanover University. He has worked at the Research and Development Department in image processing and development of SDR-based drivers in BOSCH GmbH, Hildesheim, Germany. He had three years experience with MIMOon's Research and Development Team to develop embedded signal processing and radio modules for LTE-A/4G. He is currently a Lecturer with the School of Electronics and Telecommunications, Hanoi University of Science and Technology. His research interests include resource allocation in B5G and vehicular communication systems.



THANH HIEU NGUYEN received the Ph.D. degree in electronics engineering from Chungbuk National University, Cheongju, South Korea, in 2007. He is currently a Research Fellow with the School of Electrical and Electronic Engineering, Nanyang Technological University, Singapore. His major research interests include signal processing for communications, multi-carrier, multiple-antenna systems, and vehicular communications.



TAEHYUN YOON received the B.S., M.S., and Ph.D. degrees from the School of Electronics Engineering, Kyungpook National University, in 2005, 2007, and 2015, respectively. Since 2016, he has been a Senior Researcher of the Intelligent Robotics Research Division, Electronics and Telecommunications Research Institute (ETRI), Daejeon, South Korea. His current research interests include applied mobile communication, ship-IT convergence, and LoRa networks.



WOO-SUNG JUNG received the B.S. degree in electrical and computer engineering, and M.S. and Ph.D. degrees in information and computer engineering from the School of Computer Engineering, Ajou University, South Korea, in 2007, 2009, and 2015, respectively. He is currently a Senior Researcher with the Electronics and Telecommunications Research Institute (ETRI), Daejeon, South Korea. His current research interests include wireless networking, the Internet of Things, device-to-device communication, and embedded systems.



DAESEUNG YOO received B.S., M.S., and Ph.D. degrees from the Department of Computer Engineering and Information Technology, Ulsan University, in 1998, 2001, and 2011, respectively. Since 2009, he has been a Principal Researcher of the Intelligent Robotics Research Division, Electronics and Telecommunications Research Institute (ETRI), Daejeon, South Korea. His current research interests include applied software engineering, mobile communication, ship-IT convergence, and ad-hoc networks.



SOONGHWAN RO received B.S., M.S., and Ph.D. degrees from the Department of Electronics Engineering, Korea University, in 1987, 1989, and 1993, respectively. He was a Research Engineer of the Electronics and Telecommunications Research Institute and the University of Birmingham, in 1997 and 2003, respectively. Since 1994, he has been a Professor with Kongju National University, South Korea. His research interests include 5G communication, mobile networks, and embedded systems.

...